APL Computational Physics

RESEARCH ARTICLE | MARCH 05 2026

Multiscale design of Au-based alloys for improved plasmon delivery and nanoheating in near-field transducers

Okan K. Orhan ; Frank Daniel Bello ; Nicolás Abadía ; Ortwin Hess ; John F. Donegan ; David D. O'Regan

APL Computational Physics 2, 016109 (2026)
https://doi.org/10.1063/5.0301151

APL Computational Physics ARTICLE pubs.aip.org/aip/aco

Multiscale design of Au-based alloys for improved plasmon delivery and nanoheating in near-field transducers

Cite as: APL Comput. Phys. 2, 016109 (2026); doi: 10.1063/5.0301151
Submitted: 6 September 2025 • Accepted: 10 February 2026 •
Published Online: 5 March 2026

Okan K. Orhan,[1,2] Frank Daniel Bello,[1] Nicolás Abadía,[3] Ortwin Hess,[1] John F. Donegan,[1] and David D. O'Regan[1,a)]

AFFILIATIONS

[1] School of Physics, CRANN Institute, and AMBER Research Centre, Trinity College Dublin, The University of Dublin, Dublin 2, Ireland
[2] Department of Mechanical Engineering, University of British Columbia, Vancouver, British Columbia V6T 1Z4, Canada
[3] Xtreme Photonics Lab, School of Physics and Astronomy, Cardiff University, Cardiff CF243AA, United Kingdom

[a)] **Author to whom correspondence should be addressed:** david.o.regan@tcd.ie

ABSTRACT

Plasmonic near-field transducers (NFTs) play a key role in administering nanoscale heating for a number of applications ranging from medical devices to next generation data processing technology. We present a novel multi-scale approach, combining quantum many-body perturbation theory with finite-element modeling, to predict the electric and thermal material parameters of various Au-based, noble metal (M) alloys. In particular, we focus on modeling their performance within an NFT designed to focus high-intensity, sub-diffracted light for technologies such as nanoscale etching, manipulation, sensing, and heat-assisted magnetic recording. Elemental Au is the long-standing general-purpose NFT medium due its excellent plasmonic performance at relevant wavelengths. However, elemental Au is a soft, ductile material that tends to extrude and deform in response to extreme temperature gradients. Therefore, alloying Au with other noble metals, such as Ag, Cu, Pd, or Pt, has attracted considerable interest for improved mechanical and thermal robustness while reaching threshold plasmonic generation at standard optoelectronics operating wavelengths (e.g., ≈830 nm) and approximate high-power NFT temperatures (≈400 K). We predict that certain Au–Ag alloys may offer improved thermal stability as whole-NFT media compared to elemental Au, alongside plasmonic figures of merit comparable with that of Au. Simulations of certain solid solution Au–Pd/Pt alloys enable us to predict significantly enhanced thermal conductivity. We predict that alloying with Pd at low concentrations ~10% may preserve the NFT performance of Au, while offering the benefits of improved thermal and mechanical stability.

I. INTRODUCTION

Au nano-particles and thin films are widely used in plasmonic media for opto-electronic applications, such as optical and bio-sensing,[1–3] light and heat-assisted drug delivery systems,[4–6] and data processing and recording.[7–12] This is due to their high plasmonic performance throughout the near-infrared-visible (IR-vis) spectral range.[13] However, these applications often operate at temperatures above room temperature, where dephasing rates increase and the thermal conductivity of Au decreases significantly. This can be detrimental for nanoscale components and device operation.[14] It is well known that Au is soft and may protrude or deform regardless of design and given increases in temperature as little as a few tens of Kelvin.[15] These issues may greatly reduce the thermal stability and, therefore, manufacturability of many Au-based nano-devices. Hence, alloying Au with other noble metals, such as Ag, Cu, Pd, and Pt, has been proposed to engineer both plasmonic and thermal properties for designated applications.[16–21] This is true, for example, in heat-assisted magnetic recording (HAMR), where the temperatures of near-field transducers (NFTs) may exceed 400 K.[22,23]

This present work is a proof-of-concept for a multi-scale modeling workflow that goes from beyond-density-functional theory first-principle electronic structure upward in scale. Using this, we carried out a simulated performance assessment of Au-based alloys as they fully or partially substitute the metallic components within a metal–insulator–semiconductor (MIS) NFT that was previously designed to be used in the HAMR device, as described in detail in Ref. 24. The approach developed, and the alloys explored, could, in principle, also be used to improve other NFT designs used in nano-heating applications, such as bowtie, E- or C-aperture, and a number of nanoparticle designs such as nanoparticle-on-mirror (NPoM) structures, to name a few. Since it is impractical to explore all possible alloy compositions, in what follows in this proof of principle will look at two different alloying regimes, focusing first on evaluating the plasmonic performance of mono-layer-stacked and fully disordered bulk Au–Ag/Cu alloys, followed by that of fully disordered bulk Au–Pd/Pt alloys, throughout their composition space. The multi-scale approach involves calculating first-principles electronic parameters, including quasiparticle renormalization effects at the perturbative G_0W_0 level, and then on this basis generating semi-empirical plasmonic and thermal material parameters, which in the final step are fed into finite-element method (FEM) simulations to assess NFT device-level performance of the simulated alloys.

The NFT design that we use as an example here[24] is from the context of HAMR, a next-generation high-density recording technology expected to store information on a ground-breaking scale of tens of terabytes per square inch.[9,12] The fundamental principle behind HAMR is the nanosecond-scale heating of a local region in the recording medium above its Curie temperature using sub-diffraction focused light, and by doing so, reducing coercivity of the region in order to enable magnetic recording. The key component of this operation is the near-field transducer[22,25] operating as a plasmonic antenna used for local and fast heating. Depending on the NFT, such a task typically requires either a localized surface-plasmon (LSP)[26,27] and/or a symmetric surface plasmon polariton (SPP)[28] mode at the operation wavelength. Regardless of the particular design, the heat–write–cool operation cycle has to be safely repeated many thousands of times for a viable HAMR device. For this, a sufficiently high plasmon population is required to heat the recording medium above its Curie temperature, while avoiding overheating of the metallic tip and accompanying heat sink in NFTs at the operation wavelength, for which we choose 830 nm following Ref. 24.

The NFT design in question, schematically illustrated in Fig. 1, is a plasmonic antenna designed as a MIS layered structure that supports a symmetric SPP mode.[24] The photonic Si waveguide, designed for single-mode operation, is excited with a fundamental TM mode, which subsequently couples to the MIS-NFT, producing subdiffracted light via SPP excitation. The SPP mode travels along the Au–SiO_2 interface and is funneled to the tip of the triangular antenna where nanoscale heating is generated. The NFT was designed by Abadía *et al.* for operation at 830 nm, particularly for HAMR,[29,30] and optimized to function as a Fabry–Perot plasmonic cavity (see the supplementary material for full device details).[24,31,32] For optimal HAMR operation, heating should be confined at a 50×50 nm^2 area or less on the recording medium. This is achieved by using a plasmonic tip as small as 20 nm in the cross-track (x) direction of Fig. 1.[24] The small size scale combined with the softening tendency of the elemental Au under relatively high temperatures makes the plasmonic tip potentially vulnerable to deformation. Therefore, it would be beneficial if the Au component of the nanostructure can be replaced with alloys that could significantly increase the thermal stability and hardness of the NFT, in particular at the air-bearing surface.[24,29]

The primary criterion for any NFT design is generating sufficient plasmon populations, particularly high-quality SPPs for this particular design. Two plasmonic figure-of-merits (p-FOMs) may be used to assess the propensity for SPP generation in pristine materials. The first p-FOM is the electron-energy loss spectrum (EELS) given by[34–40]

$$\mathrm{EELS} = -\Im\mathrm{m}[1/\mathscr{E}], \tag{1}$$

where $\mathscr{E} = \mathscr{E}_1 + i\mathscr{E}_2$ is the complex macroscopic dielectric function. EELS checks for a sufficient presence of nearly free electrons

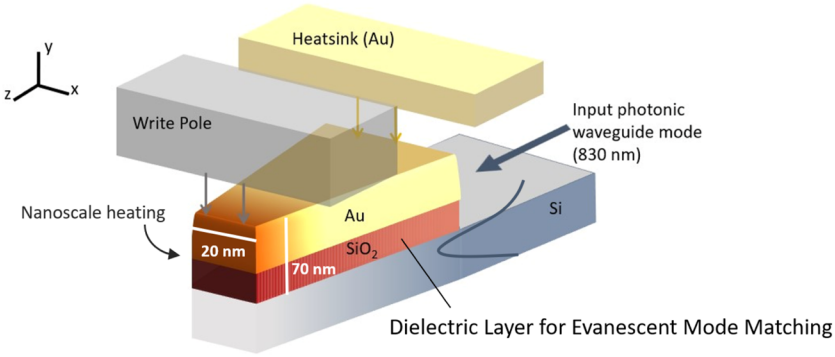

FIG. 1. Schematic diagram of the hybrid antenna-based NFT used in multi-scale simulations, as designed in Ref. 24, demonstrating the placement of the write pole and metallic heat-sink that is composed of Au or an Au alloy. The Si single-mode waveguide is designed to excite the fundamental TM mode that evanescently couples to an SPP mode with the NFT, which propagates along the Au–SiO_2 interface. The focused SPP generates nanoscale heating at the air-bearing surface (ABS) of the NFT tip, sitting only a few nanometers above the recording medium. Please see the supplementary material for full simulation details. Coupled FEM simulations of Maxwell's equations along with the heat equation were carried out.[33]

available for collective oscillations rather than forming particle–hole pairs at a given wavelength.[41] The second p-FOM is the quality of a generated SPP, indicating its longevity, given by

$$Q_{\mathrm{SPP}}(\omega) = \mathscr{E}_1^2/\mathscr{E}_2. \tag{2}$$

However, in a realistic geometry, these bulk FOM can only be indicative at best, and indeed in this study, we have used them in that spirit, helping somewhat narrow down the space of materials that we targeted for device geometry specific finite-element Maxwell's equation modeling.

We obtained the macroscopic dielectric function using the procedure defined in Ref. 42 along with thermal parameters such as thermal conductivity and heat capacity. Furthermore, we extracted the relevant quantities in the cases of ordered Au–Ag and Au–Cu alloys directly from the same work. This method is summarized in Sec. II and the description of results and optimum Au-alloys for nano-heating is provided in Sec. III.

II. THEORETICAL SPECTROSCOPY SIMULATION METHODOLOGY

A systematic illustration of the work-flow used to obtain the material parameters needed for the finite-element simulations is shown in Fig. 2. Approximate Kohn–Sham density-functional theory (KS-DFT),[43,44] which uses local and semi-local approximations for exchange and correlation,[44–47] was used for constructing an initial approximation for the band-structure. KS band-structures, in particular, offer convenient starting points for perturbative linear-response theoretical spectroscopy approaches, such as the random-phase approximation (RPA).[38–40,48] However, the accuracy of the RPA is highly dependent on the accuracy of electronic band-structure provided as its starting point, and in particular, the dressing of independent particles and holes by excitations can be important. It has been shown that KS-DFT using local-density approximations performs poorly in the case of noble metals[42,49] due to absent non-local electronic exchange–correlation effects. This error becomes more pronounced in spectral simulations, not least in the case of noble metals.[42,50–54] This can be partially overcome by providing a quasiparticle band-structure, rather than the non-interacting Kohn–Sham DFT band-structure, as the starting point for RPA. In this work, we applied a set of stretching operators, which were obtained using one-shot, non-self-consistent GW (G_0W_0)[42,55] from first principles, to the KS band-structures. The resulting stretched KS band-structures are used both in spectral simulations and determination of fundamental material parameters, such as thermal conductivity (see the supplementary material for details).

The conventional RPA operates in the product space of the occupied and unoccupied KS wave-functions, and these occupancies need to be defined with high precision. In metals, in order to accurately recover the Drude peak generated by intra-band transitions within the RPA, an unfeasibly dense Brillouin zone sampling of the Fermi surface is required.[56] As a result, and following established practice in this area, in this work the Drude plasmon contribution (also called the intra-band contribution) to the macroscopic dielectric function ($\mathscr{E}$) is included via the Drude–Lorentz classical model,[57–60] where it is given by

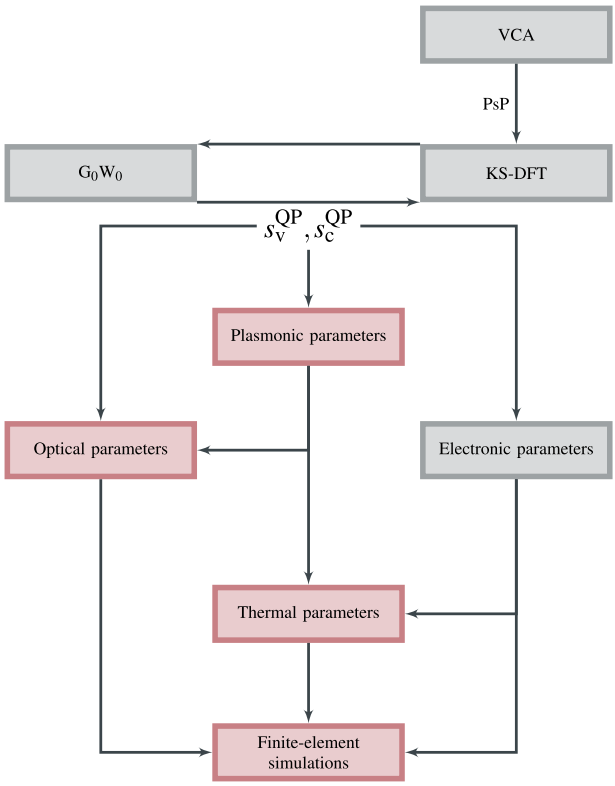

FIG. 2. Schematic illustration of the work-flow followed here to obtain the material parameters for finite-element simulations. The virtual crystal approximation (VCA) is used to model virtual atoms of Au alloys with pseudo-potentials (PsP), which are then fed into the approximate Kohn–Sham density-functional theory (KS-DFT). Band stretching factors (s_v^{QP} and s_c^{QP}) are then obtained by means of linear regression to quasiparticle energies calculated using one-shot non-self-consistent many-body perturbation theory (G_0W_0). Please see Sec. II for details. Color codes are assigned to the first-principles parameters as gray and the semi-empirical parameters as pink. See the supplementary material for full lists of parameters used and details of the computational methodology.

$$\mathscr{E}^{\mathrm{intra}}(\omega) = \varepsilon_\infty - \frac{\omega_p^2}{\omega^2 - i\eta_p\omega}. \tag{3}$$

Here, ω_p, η_p, and ε_∞ are the Drude plasmon energy, the phenomenological inverse lifetime, and the electric permittivity at the infinite-frequency limit, respectively. In order to construct a practical multi-scale work-flow appropriate to materials exploration and interpolation, a phenomenological inverse lifetime and the electric permittivity are determined from the experimental spectra of the elemental metals in the infra-red region.

For a uniform, non-interacting electron gas, the Drude plasmon energy can be approximated by[57,58,61]

$$\omega_p^2 = \frac{4\pi N(E_F)}{m_{\mathrm{eff}}}, \tag{4}$$

where $N(E_F)$ is the density of states (DOS) at the Fermi level and m_{eff} is the electron effective mass. The Drude plasmon energy can,

however, be calculated within first principles starting from the electronic band structure using one-band theory.[62] Within the one-band theory, the effective mass of the metallic band is defined by assuming that these bands have a parabolic dispersion to the Fermi surface given by[62]

$$m_{\text{eff}}^{-1} \approx \frac{1}{3}\langle v^2(E_{\text{F}})\rangle = \frac{1}{3}\left(\sum_i \int_{S_{\text{F}_i}} d\mathbf{k}\, v_i^2(\mathbf{k})\right)\left(\sum_j \int_{S_{\text{F}_j}} d\mathbf{k}'\right)^{-1}, \quad \text{if} \quad v_i^2(\mathbf{k}) = \left|\frac{\partial E_{i,\mathbf{k}}}{\partial \mathbf{k}}\right|^2, \tag{5}$$

where S_{F_i} is the Fermi surface of the i^{th} metallic band. This yields a Drude plasmon energy that can be approximated as

$$\omega_{\text{p}}^2 = \frac{4\pi}{3} N(E_{\text{F}})\langle v^2(E_{\text{F}})\rangle. \tag{6}$$

Our work finds that Au–Ag binary alloys form continuous face-centered cubic (FCC) solids for any given stoichiometric ratio, rather than an ordered alloy. This is because they exhibit only short-range ordering.[63] While the Au–Cu alloys also prefer the continuous FCC phase, Au_3Cu, AuCu, and $AuCu_3$ show ordered structures at ≈400 – 700 K.[64] Similarly, Au_3Pd and $AuPd_3$ at ≈900 – 1110 K as well as AuPd at ≈300 – 400 K show ordered structures, with the continuous FCC phase being a general trend for other stoichiometric ratios and temperature ranges.[65] In the case of the Au–Pt alloys, there is a large miscibility gap, where Au and Pt forms local sub-structures for $\gtrapprox$ %15 ratio of Pt at the lower temperatures; however, there is still the continuous FCC phase of the low-concentration Pt alloys at ≈400 K, and high-concentration Pt alloys exist in a very narrow temperature belt between the miscibility and liquid phase regions of higher temperatures.[66] Hence, most of the Au–M alloys in this work have continuous FCC solid solutions without long-range ordering. The most comprehensive approach would be to achieve statistical averaging of every possible spatial configuration within a quite large cell, namely, the super-cell approximation, to be able to include the disorder in such alloys. However, it is not feasible for high-throughput simulations, much less those involving many-body perturbation theory. An expedient, if approximate, approach, instead, is to replace the Au–M atom pairs with a virtual atom, which interpolates the behaviors of original atoms, namely, the virtual crystal approximation (VCA).[67,68] This can be applied within the approximate KS-DFT via a mixing scheme for the pseudo-potential (PsP) of the virtual atom using the constituting atoms A and B, given by[68]

$$V_{\text{PsP}}^{\text{virtual}}(\mathbf{r},\mathbf{r}') = (1-x)V_{\text{PsP}}^{\text{A}}(\mathbf{r},\mathbf{r}') + xV_{\text{PsP}}^{\text{B}}(\mathbf{r},\mathbf{r}'). \tag{7}$$

Here, "x" refers to the amount of alloyed metal. The VCA provides a simple scheme for fully disordered case, which excludes any ordering, both long-range and short-range.

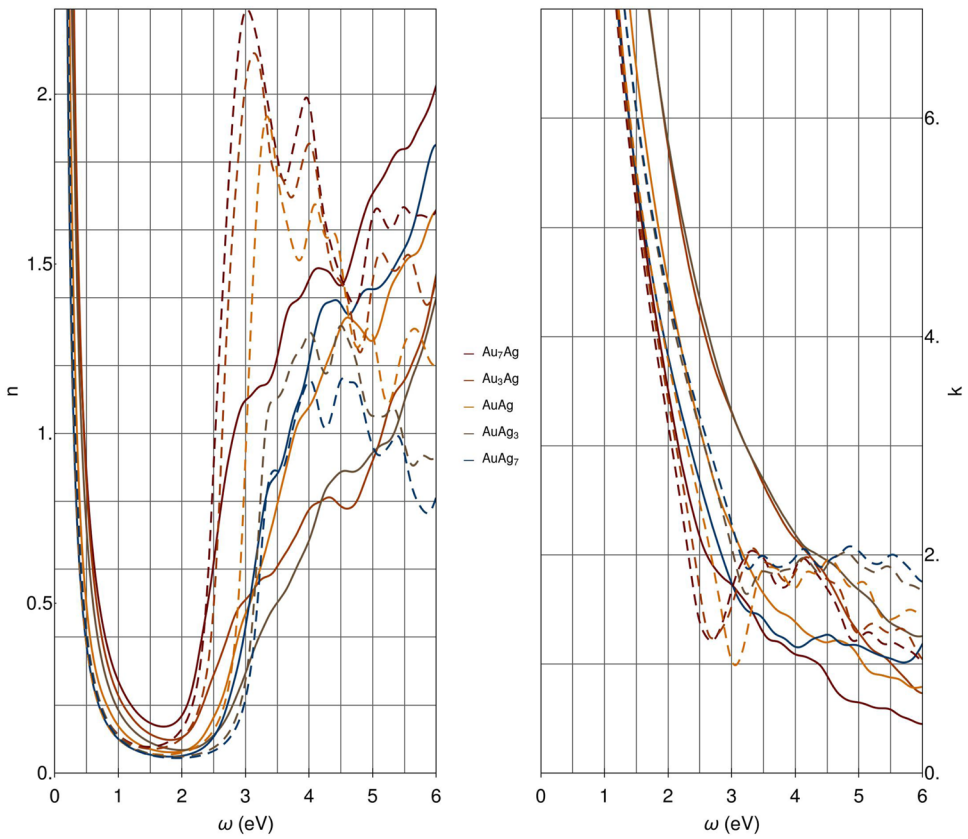

FIG. 3. Simulated refractive indices (n) and extinction coefficients (k) for the mono-layer-stacked ordered (solid curves) and fully disordered (dashed) Au–Ag alloy series. Simulation methodology, described here and in Ref. 42, comprises density-functional theory, many-body perturbation theory including exciton binding within the one-shot G_0W_0, and RPA approximations, including local-field effects, together with a semi-empirical interpolation scheme for Drude model parameters for the intra-band (low-energy) regime. Fully disordered alloying is simulated within the virtual crystal approximation.

III. RESULTS

Alloying permits frequency-dependent optical properties to be achieved that are different to those of the parent metals and certainly beyond just their linear interpolation. Our results show, however, that the strength of this change depends on the driving frequency and also on whether ordered or disordered alloying is present. Figure 3 shows a representative set of simulated refractive indices (n) and extinction coefficients (k) for the mono-layer-stacked ordered (solid curves) and fully disordered (dashed) Au–Ag alloy series. Here, we see that at certain frequencies, particularly in the inter-band (higher-energy, post-Drude) regime, the alloy-composition dependence can counter-intuitively be stronger in the disordered alloying case, on the basis of our simulations. Such spectra depend intricately on the precise details of the electronic bandstructure and how that is calculated, and then, the theory used to capture interactions between electron–hole pairs and the applied field.

The corresponding plot to Fig. 3 for the Au–Cu alloy series is provided in the supplementary material. Focusing our attention to our aforementioned target incident wavelength of 830 nm (just below 1.5 eV in vacuum), we find that the alloy composition dependence is much more modest (precise values are provided in the supplementary material). The ordered alloys in this near-infrared regime tend to show higher n and k values, based on simulation, but not at all composition values. These figures convey the qualitative result that the variation with respect to wavelength is rather subtle (particularly for n) in the near-infrared wavelength regime, and while there may be performance gains available through varying the incident wavelength, unless significant changes are made, this may be slight compared to that gained through alloying, among other factors. In some of our previously reported work from Ref. 42, we considered three significantly different wavelengths, but only regarding bulk optical properties and while mixing fewer metals in simulation. For the remainder of the present work, we will restrict our attention to incident light at 830 nm.

Despite being a well-known plasmonic metal, elemental Ag produces weaker plasmons than Au at 830 nm, indicated by its normalized EELS amplitude shown in Fig. 4(a), (left), as it has a single and narrow plasmonic peak at ~330 nm.[42] However, the small population of SPPs of Ag-rich alloys is longer lived compared to that of elemental Au, as shown in Fig. 4(a), (right). Interestingly, the mono-layer-stacked $AuAg_3$ exhibits exceptionally high-quality SPPs, while still exhibiting significant simulated generation. Furthermore, it has a predicted thermal conductivity of $\kappa = 669$ (W m^{-1} K^{-1}), significantly higher than the $\kappa = 312$ (W m^{-1} K^{-1}) of the elemental Au. To calculate the conductivity, our predictions include various semi-empirically approximated scattering processes, such as the electron–phonon, the electron–electron, and the electron-impurity scattering, and subsequently also calculated the specific heat capacity for FEM simulations of the heat equation (see the supplementary material for details and values).

The elemental metals Au and Cu exhibit rather similar affinities for SPP generation. Disordered Au_xCu_{1-x} alloys produce lower quality SPPs, shown in Fig. 4(b), regardless of the fractional ratios. On the other hand, mono-layer-stacked Au_3Cu, AuCu, and $AuCu_3$ show improved qualities in simulation, with strong plasmons and improved thermal conductivities compared to both the elemental Au and Cu (see the supplementary material). As shown in Fig. 4(c),

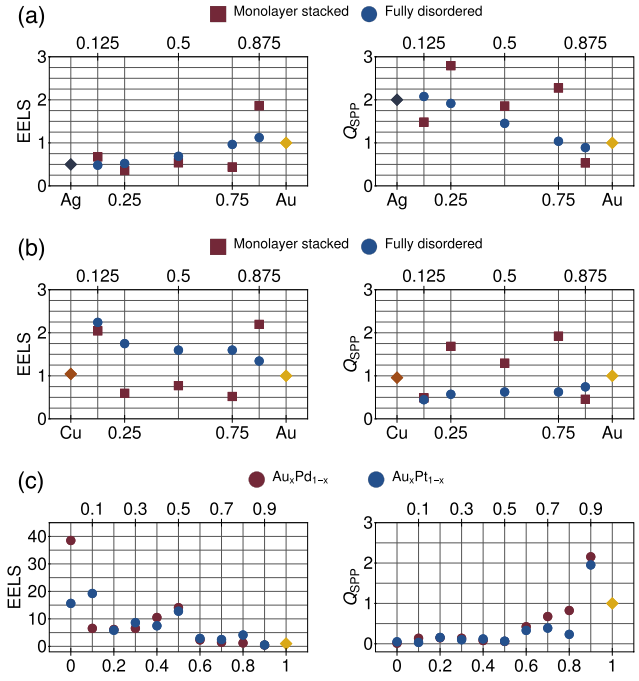

FIG. 4. Amplitudes at 830 nm of electron energy-loss (left column) and the surface-plasmon polariton quality factor (right column) of row (a): the mono-layer-stacked and fully disordered Au–Ag alloys; row (b): mono-layer-stacked and fully disordered Au–Cu alloys, and row (c): fully disordered Au–Pd/Pt alloys. All values are normalized against the elemental Au values, which are set to a value of 1. The ordered Au–Ag and Au–Cu alloy cases were extracted from Ref. 42, for which the matching fractional stoichiometric ratios for the fully ordered were chosen.

Pd- and Pt-rich alloys produce strong, but quite short-living plasmons. On the contrary, Au-rich fully disordered Au–Pd/Pt improve the SPP qualities significantly. Unfortunately, mixing Au with either Pd or Pt appears to substantially reduce thermal conductivity, unsurprisingly as the elemental Pd and Pt are relatively poor thermally conductive materials. For the avoidance of doubt, we emphasize here that alloy scattering is not considered in our calculations, which can only diminish thermal conductivity.

We performed FEM simulations using the candidate alloys with potentially promising plasmon generation and improved thermal conductivity, following initial screening. In the NFT design, SPPs are generated by using a threefold process, namely, (1) effective index matching, for a photonic waveguide mode with the plasmonic mode, done by adjusting the thickness of the insulator layer, (2) designing the MIS waveguide component as a Fabry–Perot cavity, and (3) tapering to achieve localized heating suitable in media for HAMR. In Figs. 5(b) and 5(c), we show the temperature, heat flux, and thermal gradients magnitude of the NFT and within the center of a FePt magnetic layer often used in recording media (see the supplementary material for full media materials/dimensions). The size of the heated region may be controlled by adjusting the input power where the bulk of the power within the NFT is seen to be concentrated within the tip of the NFT (red region).[69] This is vital for maximizing areal bit densities in magnetic recording devices,

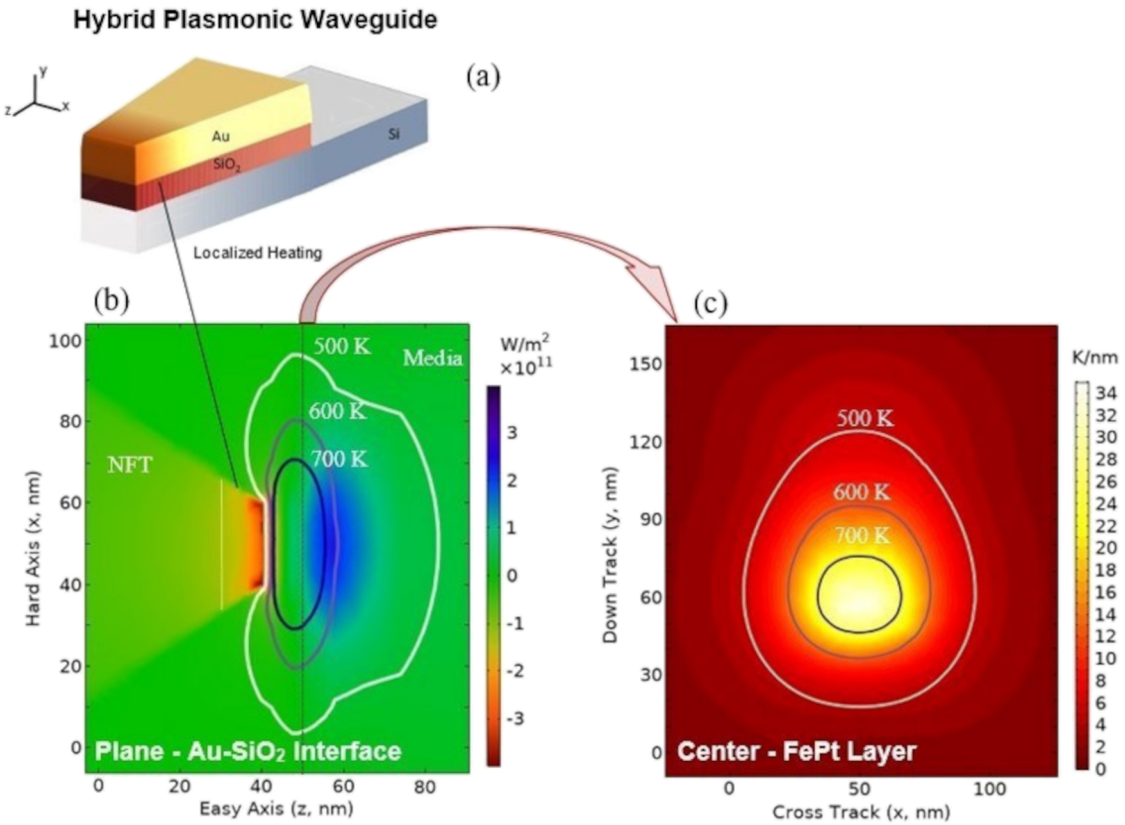

FIG. 5. (a) Minimal model of an M-I-S hybrid plasmonic waveguide suitable as an NFT for HAMR, from Ref. 24. The air-bearing surface (ABS) is 20 nm along the x-direction (cross track) and 70 nm (Au + SiO_2) in the y-direction (down track). See the supplementary material for a full list of dimensions. (b) Planar cross section taken from the metal–insulator interface showing the location of maximum heat flux (W/m^2), the z-component, i.e., easy axis component of which is shown on the color scale. AuPt/Pd alloys with concentrations of Pd/Pt of 30%, 50%, or 70% were simulated in the NFT region with the highest power per unit area (demarked by the white dotted line), where softening of the Au may occur given temperatures circa 400 K. (c) Cross section from the center of the recording layer [black vertical line in panel (b)] located 13.5 nm away from the ABS, showing temperatures reaching above typical values for the Curie temperature of FePt. The magnitude of the temperature gradient is also plotted with maximum cross- and down-track values listed in Table I. We note that no temperature-related boundary conditions are imposed on the NFT or heatsink within thermal simulations. Only the outermost boundaries of the simulation are set to room temperature, 293.15 K, with a minimum air gap of 35 nm to the heatsink. The fixed-temperature boundaries are very well-separated from the NFT. See the supplementary material for surface profiles of the temperature distribution through the NFT.

particularly due to the relatively strong cross (x axis) and down (y) track gradients produced in the media. This reduces heating of adjacent bits, thus preventing overwriting.

Table I contains a comparative analysis of the thermal performance[22] when replacing the Au components with various Au alloys as well as the last 10 nm section from the ABS. Figure of merits used to quantify the thermal performance of the NFT are adopted from Refs. 22 and 24. The dimensions of the NFT design used in simulations, being originally optimized using pure Au, are left unchanged. Therefore, we notice comparable optical performance (required input power, P_{in}) using alloys with similar refractive indices to Au. We find that in order to simultaneously have an improved thermal performance, alloys that have larger thermal conductivities than pure Au are desired. Therefore, Table I reports on a number of Au_xAg_{1-x} alloys used to replace the entire metallic section of the NFT with a noticeable effect. In particular, a crucial figure of merit for thermal stability, which compares the change in FePt temperature to that of the Au in the NFT ($\Delta T_{Media}/\Delta T_{Au}$), is markedly improved. The values for maximum temperature in the metallic component of the NFT (T^{max}_{metal}) lies within the bright orange/red region of Fig. 4(b), while the maximum temperature of the FePt layer (T^{max}_{FePt}) lies just to the left of the blue region [contours of Fig. 4(c)]. While their exact positions may vary by a few nanometers, both areas are regions of maximum heat flux, i.e., heat transport. It should also be noted that thermal gradients in the recording layer, a crucial figure of merit for bit density, tend to be larger for Au alloys that index match well with pure Au and more effectively localize power within the recording layer, i.e., more effectively demonstrate better optical efficiency.

Au alloyed with a small percentage (10%) of Pt/Pd, which are expected to have improved hardness by the rule of mixing, also performed well by demonstrating in simulation a similar figure of merit for thermal stability to that of pure Au. However, for alloys with higher concentrations of Pd/Pt, replacing the entire metallic

TABLE I. Simulated thermal efficiency of NFT with a tapered, hybrid plasmonic waveguide[24] using various Au-alloys. Here, temperature less than 400 K is considered desirable for Au while maximizing the temperature in the media. High thermal gradients are also considered desirable here in order to localize the heating as much as possible. The reported values for the refractive index of Au vary, and the value used here for Au of $n \approx 0.068$ is derived from first principles. Thermal conductivity values (κ) are semi-empirically derived for each alloy (see the supplementary material for details).

	κ (W m^{-1} K^{-1})	$\Delta T_{FePt}/\Delta T_{metal}$	T^{max}_{metal} (K)	T^{max}_{FePt} (K)	Max. cross. track grad. (K/nm)	Max. downtrack grad. (K/nm)
Alloying of the metallic section of NFT and heat-sink for optimized nanoheating figures of merit						
(Au), $n \approx 0.068$, P_{in} = 3.75 mW	312	6.2	389	891	16.7	17.6
($AuAg_7$) P_{in} = 4.00 mW	347.9	6.5	381	867	15.3	16.0
($AuAg_3$) P_{in} = 6.75 mW	669.2	7.1	376	885	11.7	10.8
($Au_{0.125}Ag_{0.875}$) P_{in} = 4.50 mW	469	7.0	381	911	15.3	15.7
($Au_{0.9}Pd_{0.1}$) P_{in} = 6.50 mW	488.5	6.2	393	911	11.3	15.4
Alloying 10 nm tip of the metallic section						
(Pd) P_{in} = 3.75 mW	75	3.0	418	668	8.1	9.4
($Au_{0.5}Pd_{0.5}$) P_{in} = 3.75 mW	143.7	4.5	393 (436 in the alloy section)	740	9.8	11.3
($Au_{0.3}Pt_{0.7}$) P_{in} = 4.25 mW	179.1	4.7	402 (432 in the alloy section)	800	10.8	12.5
($Au_{0.7}Pt_{0.3}$) P_{in} = 4.25 mW	602	4.8	393 (402 in the alloy section)	775	9.4	11.1

component yielded a lower optical and thermally efficiency in simulation due to poorer index matching between photonic and plasmonic modes. However, they were simulated to be potentially suitable for transducer operation when replacing a smaller section near the tip of the NFT, where the majority of power is concentrated. Although optical and thermal efficiency was lower, these alloys are anticipated to have smaller coefficients of expansion.

IV. CONCLUSIONS

To conclude, we have calculated electronic and thermal material parameters used to measure the plasmonic performance for Au–M alloys suitable for nanoheating applications. By substituting, fully or partially, the metallic parts of a previously introduced model NFT design, we demonstrate that plasmonic performance is generally maintained or reduced at 830 nm. However, it potentially enables the engineering of desired thermal performance of Au-based NFTs and possibly improved mechanical durability under relatively high-power conditions. We presented the multiscale design protocol as a proof-of-concept within a representative, previously demonstrated NFT design; however, it is suitable to be modified for a number of nanoscale heating applications. Despite our focus on a single operation wavelength and temperature, our assessment procedure is easily applicable to any wavelength, miscible combinations of metals, and reasonable temperature at which phonon contributions are relatively small in those.

SUPPLEMENTARY MATERIAL

We refer the reader to the supplementary material that provides details of computational methodology; the semi-empirical thermal parameters used; the optimized first-principles simulation parameters; and the thermal, optical, and finite-element simulation parameters used.

ACKNOWLEDGMENTS

We acknowledge the support from the Trinity College Dublin School of Physics, Taighde-Éireann–Research Ireland through the Advanced Materials and Bioengineering Research Centre (AMBER, Grant Nos. 12/RC/2278, 12/RC/2278_P2, and 15/IA/2854), the European Regional Development Fund (ERDF), and the EU Horizon 2020 - Marie Skłodowska-Curie Grant No. 713567. The work of NA was supported by the Engineering and Physical Sciences Research Council (Grant No. EP/X011917/1), (Grant No. EP/Y00082X/1). We also acknowledge the DJEI/DES/SFI/HEA Irish Centre for High-End Computing (ICHEC) for the provision of computational facilities and support. We further acknowledge Trinity Centre for High Performance Computing and the Science Foundation Ireland for the maintenance and funding, respectively, of the Boyle cluster on which further calculations were performed.

AUTHOR DECLARATIONS

Conflict of Interest

The authors have no conflicts to disclose.

Author Contributions

Okan K. Orhan: Conceptualization (equal); Data curation (equal); Formal analysis (equal); Investigation (equal); Software (equal); Visualization (equal); Writing – original draft (equal). **Frank Daniel Bello**: Conceptualization (equal); Data curation (equal); Formal analysis (equal); Investigation (equal); Software (equal); Visualization (equal); Writing – review & editing (equal). **Nicolás Abadía**: Data curation (equal); Investigation (equal); Methodology (equal). **Ortwin Hess**: Funding acquisition (equal); Project administration (equal). **John F. Donegan**: Conceptualization (equal); Funding acquisition (equal); Project administration (equal); Supervision (equal); Writing – review & editing (equal). **David D.**

O'Regan: Conceptualization (equal); Methodology (equal); Project administration (equal); Resources (equal); Supervision (equal); Writing – review & editing (equal).

DATA AVAILABILITY

The data that support the findings of this study are available within the article and its supplementary material.

REFERENCES

[1] M. Alagiri, P. Rameshkumar, and A. Pandikumar, "Gold nanorod-based electrochemical sensing of small biomolecules: A review," Microchim. Acta **184**, 3069–3092 (2017).

[2] S. Bengali and M. Giri, "Gold sensor," U.S. patent App. 15/749,036 (2018).

[3] M. S. Rodrigues, D. Costa, R. P. Domingues, M. Apreutesei, P. Pedrosa, N. Martin, V. M. Correlo, R. L. Reis, E. Alves, N. P. Barradas, P. Sampaio, J. Borges, and F. Vaz, "Optimization of nanocomposite Au/TiO_2 thin films towards LSPR optical-sensing," Appl. Surf. Sci. **438**, 74–83 (2018), part of Special Issue: 10th International Conference on Materials Science and Engineering.

[4] P. K. Jain, I. H. El-Sayed, and M. A. El-Sayed, "Au nanoparticles target cancer," Nano Today **2**, 18–29 (2007).

[5] X. Zhang, "Gold nanoparticles: Recent advances in the biomedical applications," Cell Biochem. Biophys. **72**, 771–775 (2015).

[6] S. Tran, P.-J. DeGiovanni, B. Piel, and P. Rai, "Cancer nanomedicine: A review of recent success in drug delivery," Clin. Transl. Med. **6**, 44 (2017).

[7] F. Bello, N. Kongsuwan, J. F. Donegan, and O. Hess, "Controlled cavity-free, single-photon emission and bipartite entanglement of near-field-excited quantum emitters," Nano Lett. **20**, 5830–5836 (2020).

[8] F. Bello, S. Sanvito, O. Hess, and J. F. Donegan, "Shaping and storing magnetic data using pulsed plasmonic nanoheating and spin-transfer torque," ACS Photonics **6**, 1524–1532 (2019).

[9] C. Black, S. Gates, C. Murray, and S. Sun, Magnetic storage medium formed of nanoparticles, 2000.

[10] M. Mansuripur, A. R. Zakharian, A. Lesuffleur, S.-H. Oh, R. J. Jones, N. C. Lindquist, H. Im, A. Kobyakov, and J. V. Moloney, "Plasmonic nano-structures for optical data storage," Opt. Express **17**, 14001–14014 (2009).

[11] I. Sato, T. Oike, and N. Hanashima, "Heat assisted magnetic recording head and heat assisted magnetic recording apparatus for heating a recording region in a magnetic recording medium during magnetic recording," U.S. patent 7,538,978 (2009).

[12] J. Zou, K. Gao, W. Challener, M. Ostrowski, V. Inturi, T. Zhao, and M. Kautzky, Recording head for heat assisted magnetic recording with diffusion barrier surrounding a near field transducer, 2014.

[13] V. Amendola, R. Pilot, M. Frasconi, O. M. Maragò, and M. A. Iatì, "Surface plasmon resonance in gold nanoparticles: A review," J. Phys.: Condens. Matter **29**, 203002 (2017).

[14] N. Bodenschatz, A. Liemert, S. Schnurr, U. Wiedwald, and P. Ziemann, "Extending the 3ω method: Thermal conductivity characterization of thin films," Rev. Sci. Instrum. **84**, 084904 (2013).

[15] W. M. Abbott, C. P. Murray, C. Zhong, C. Smith, C. McGuinness, E. Rezvani, C. Downing, D. Daly, A. K. Petford-Long, F. Bello, D. McCloskey, and J. F. Donegan, "Less is more: Improved thermal stability and plasmonic response in Au films via the use of subnanometer Ti adhesion layers," ACS Appl. Mater. Interfaces **11**, 7607–7614 (2019).

[16] M. G. Blaber, M. D. Arnold, and M. J. Ford, "A review of the optical properties of alloys and intermetallics for plasmonics," J. Phys.: Condens. Matter **22**, 143201 (2010).

[17] B. Dastmalchi, P. Tassin, T. Koschny, and C. M. Soukoulis, "A new perspective on plasmonics: Confinement and propagation length of surface plasmons for different materials and geometries," Adv. Opt. Mater. **4**, 177–184 (2016).

[18] D. Beaglehole and E. Erlbach, "Electronic structure of noble-metal-noble-metal alloys," Phys. Rev. B **6**, 1209–1225 (1972).

[19] Y. Nishijima, Y. Hashimoto, G. Seniutinas, L. Rosa, and S. Juodkazis, "Engineering gold alloys for plasmonics," Appl. Phys. A **117**, 641–645 (2014).

[20] C. Gong and M. S. Leite, "Noble metal alloys for plasmonics," ACS Photonics **3**, 507–513 (2016).

[21] Y. Hashimoto, G. Seniutinas, A. Balčytis, S. Juodkazis, and Y. Nishijima, "Au-Ag-Cu nano-alloys: Tailoring of permittivity," Sci. Rep. **6**, 25010 (2016).

[22] A. Datta and X. Xu, "Comparative study of optical near-field transducers for heat-assisted magnetic recording," Opt. Eng. **56**, 121906 (2017).

[23] F. Bello, D. Wolf, G. J. Parker, C. Wolf, A. Krichevsky, F. Zong, N. Abadía, and J. F. Donegan, "Optical, thermal, and bit-writing analysis of a directly coupled plasmonic waveguide for heat-assisted magnetic recording," OSA Continuum **3**, 2010–2021 (2020).

[24] N. Abadía, F. Bello, C. Zhong, P. Flanigan, D. M. McCloskey, C. Wolf, A. Krichevsky, D. Wolf, F. Zong, A. Samani, D. V. Plant, and J. F. Donegan, "Optical and thermal analysis of the light-heat conversion process employing an antenna-based hybrid plasmonic waveguide for HAMR," Opt. Express **26**, 1752–1765 (2018).

[25] H. Yang, J. Li, and G. Xiao, "Decay and propagation properties of symmetric surface plasmon polariton mode in metal-insulator-metal waveguide," Opt. Commun. **395**, 159–162 (2017), part of Special Issue: Nano-Optoelectronics: Advanced Optoelectronic Devices Based on Nanostructures and Nanomaterials.

[26] C. Sönnichsen, T. Franzl, T. Wilk, G. v. Plessen, and J. Feldmann, "Plasmon resonances in large noble-metal clusters," New J. Phys. **4**, 93 (2002).

[27] A. J. Haes, S. Zou, G. C. Schatz, and R. P. Van Duyne, "A nanoscale optical biosensor: The long range distance dependence of the localized surface plasmon resonance of noble metal nanoparticles," J. Phys. Chem. B **108**, 109–116 (2004).

[28] A. V. Zayats, I. I. Smolyaninov, and A. A. Maradudin, "Nano-optics of surface plasmon polaritons," Phys. Rep. **408**, 131–314 (2005).

[29] V. Krishnamurthy, D. K. T. Ng, K. P. Lim, and Q. Wang, "Efficient integrated light-delivery system design for HAMR: Maximal optical coupling for transducer and nanowaveguide," IEEE Trans. Magn. **52**, 3000507 (2016).

[30] C. Zhong, P. Flanigan, N. Abadía, F. Bello, B. D. Jennings, G. Atcheson, J. Li, J.-Y. Zheng, J. J. Wang, R. Hobbs, D. McCloskey, and J. F. Donegan, "Effective heat dissipation in an adiabatic near-field transducer for HAMR," Opt. Express **26**, 18842–18854 (2018).

[31] G. Singh, V. Krishnamurthy, J. Pu, and Q. Wang, "Efficient plasmonic transducer for nanoscale optical energy transfer in heat-assisted magnetic recording," J. Lightwave Technol. **32**, 3074–3080 (2014).

[32] A. Krichevsky, C. B. Wolf, F. D. Bello, K. E. Ballantine, J. Donegan, and D. M. O. McCloskey, "Method and system for reducing undesirable reflections in a HAMR write apparatus," U.S. patent 9484051 (2016).

[33] C AB, COMSOL multiphysics® v. 5.4, Stockholm, Sweden.

[34] H. Boersch, H. Miessner, and W. Raith, "Untersuchungen zur winkelabhängigkeit des 14,7 ev-energieverlustes von elektronen in aluminium," Z. Phys. **168**, 404–410 (1962).

[35] H. Raether, "Solid state excitations by electrons," in *Springer Tracts in Modern Physics* (Springer, Berlin, 1965), Vol. 38, pp. 84–157.

[36] H. Froitzheim, *Electron Energy Loss Spectroscopy*, in *Electron Spectroscopy for Surface Analysis*, edited by H. Ibach (Springer, Berlin, Heidelberg, 1977), pp. 205–250.

[37] R. A. Ferrell, "Angular dependence of the characteristic energy loss of electrons passing through metal foils," Phys. Rev. **101**, 554–563 (1956).

[38] D. Bohm and D. Pines, "A collective description of electron interactions. I. Magnetic interactions," Phys. Rev. **82**, 625–634 (1951).

[39] D. Pines and D. Bohm, "A collective description of electron interactions: II. Collective vs individual particle aspects of the interactions," Phys. Rev. **85**, 338–353 (1952).

[40] D. Bohm and D. Pines, "A collective description of electron interactions: III. Coulomb interactions in a degenerate electron gas," Phys. Rev. **92**, 609–625 (1953).

[41] M. Rocca, "Low-energy eels investigation of surface electronic excitations on metals," Surf. Sci. Rep. **22**, 1–71 (1995).

[42] O. K. Orhan and D. D. O'Regan, "Plasmonic performance of $Au_xAg_yCu_{1-x-y}$ alloys from many-body perturbation theory," J. Phys.: Condens. Matter **31**, 315901 (2019).

[43] P. Hohenberg and W. Kohn, "Inhomogeneous electron gas," Phys. Rev. **136**, B864–B871 (1964).

[44]W. Kohn and L. J. Sham, "Self-consistent equations including exchange and correlation effects," Phys. Rev. **140**, A1133–A1138 (1965).
[45]D. C. Langreth and J. P. Perdew, "Theory of nonuniform electronic systems. I. Analysis of the gradient approximation and a generalization that works," Phys. Rev. B **21**, 5469–5493 (1980).
[46]J. P. Perdew, "Density-functional approximation for the correlation energy of the inhomogeneous electron gas," Phys. Rev. B **33**, 8822–8824 (1986).
[47]J. P. Perdew, J. A. Chevary, S. H. Vosko, K. A. Jackson, M. R. Pederson, D. J. Singh, and C. Fiolhais, "Atoms, molecules, solids, and surfaces: Applications of the generalized gradient approximation for exchange and correlation," Phys. Rev. B **46**, 6671–6687 (1992).
[48]A. D. McLacham and M. A. Ball, "Time-dependent Hartree–Fock theory for molecules," Rev. Mod. Phys. **36**, 844–855 (1964).
[49]T. Rangel, D. Kecik, P. E. Trevisanutto, G.-M. Rignanese, H. Van Swygenhoven, and V. Olevano, "Band structure of gold from many-body perturbation theory," Phys. Rev. B **86**, 125125 (2012).
[50]H. Eckardt, L. Fritsche, and J. Noffke, "Self-consistent relativistic band structure of the noble metals," J. Phys. F: Met. Phys. **14**, 97 (1984).
[51]A. J. Cohen, P. Mori-Sánchez, and W. Yang, "Challenges for density functional theory," Chem. Rev. **112**, 289–320 (2012).
[52]A. Marini, G. Onida, and R. Del Sole, "Quasiparticle electronic structure of copper in the *GW* approximation," Phys. Rev. Lett. **88**, 016403 (2001).
[53]A. Marini, R. Del Sole, and G. Onida, "First-principles calculation of the plasmon resonance and of the reflectance spectrum of silver in the GW approximation," Phys. Rev. B **66**, 115101 (2002).
[54]A. Marini, R. Del Sole, A. Rubio, and G. Onida, "Quasiparticle band-structure effects on the d hole lifetimes of copper within the GW approximation," Phys. Rev. B **66**, 161104 (2002).
[55]A. Marini, C. Hogan, M. Grüning, and D. Varsano, "yambo: An ab initio tool for excited state calculations," Comput. Phys. Commun. **180**, 1392–1403 (2009).
[56]A. Marini, "Optical and electronic properties of copper and silver: From density functional theory to many body effects," Ph.D. thesis, University of Rome-Tor Vergata, 2001.
[57]P. Drude, "Zur elektronentheorie der metalle," Ann. Phys. **306**, 566–613 (1900).
[58]P. Drude, "Zur elektronentheorie der metalle; II. Teil. Galvanomagnetische und thermomagnetische effecte," Ann. Phys. **308**, 369–402 (1900).
[59]H. A. Lorentz, *The Theory of Electrons and Its Applications to the Phenomena of Light and Radiant Heat: A Course of Lectures Delivered in Columbia University in March and April, 1906* (Columbia University Press, New York, 1909), Vol. 29.
[60]M. Fox, *Optical Properties of Solids* (Oxford University Press, 2010), Vol. 3.
[61]R. T. Beach and R. W. Christy, "Electron-electron scattering in the intraband optical conductivity of Cu, Ag, and Au," Phys. Rev. B **16**, 5277–5284 (1977).
[62]M. H. Cohen, "Optical constants, heat capacity and the fermi surface," Philos. Mag. **3**, 762–775 (1958).
[63]H. Okamoto and T. B. Massalski, "The Ag–Au (silver-gold) system," Bull. Alloy Phase Diagrams **4**, 30 (1983).
[64]H. Okamoto, D. J. Chakrabarti, D. E. Laughlin, and T. B. Massalski, "The Au-Cu (gold-copper) system," J. Phase Equilib. **8**, 454 (1987).
[65]H. Okamoto and T. B. Massalski, "The Au-Pd (gold-palladium) system," Bull. Alloy Phase Diagrams **6**, 229–235 (1985).
[66]H. Okamoto and T. B. Massalski, "The Au-Pt (gold-platinum) system," Bull. Alloy Phase Diagrams **6**, 46–56 (1985).
[67]L. Nordheim, "Zur elektronentheorie der metalle. I," Ann. Phys. **401**, 607–640 (1931).
[68]L. Bellaiche and D. Vanderbilt, "Virtual crystal approximation revisited: Application to dielectric and piezoelectric properties of perovskites," Phys. Rev. B **61**, 7877–7882 (2000).
[69]F. Bello, O. K. Orhan, N. Abadía, D. D. O'Regan, and J. F. Donegan, "Material characterization and thermal performance of Au alloys in a thin-film plasmonic waveguide," in *Conference on Lasers and Electro-Optics* (Optical Society of America, 2019), p. JTu2A.110.